Technical University of Denmark

DTU

Chaotic Vibrations of Non shallow Arches

Thomsen, Jon Juel

Published in:
Journal of Sound and Vibration

Publication date:
1992

Document Version
Publisher's PDF, also known as Version of record

Link back to DTU Orbit

DTU Library
Technical Information Center of Denmark

CHAOTIC VIBRATIONS OF NON-SHALLOW ARCHES

J. J. Thomsen

Department of Solid Mechanics, The Technical University of Denmark, DK-2800 Lyngby, Denmark

Non-shallow arches inherently possess a nearly two-to-one internal resonance between the lowest modes of symmetric and antisymmetric vibration. This implies that non-linear modal interaction may entirely dominate the dynamic response, even at extremely small excitation levels. In this paper the effects of such non-linearities are studied by perturbation analysis and numerical simulations. Special emphasis is laid on chaotic vibrations, which are shown to occur for excitation levels and frequencies occupying significant areas of the primary region of dynamic instability. Thus, this is a case of a structure in widespread practical use, which may display unpredictable chaotic behaviour not very far from normal operating conditions. Evidence for chaotic motion is given through Poincaré sections, frequency spectres and Lyapunov exponents. The routes to chaos are shown to include quasi-periodic break-up, intermittency and long transients.

1. INTRODUCTION

In the 1950s Bolotin [1] studied the parametrically excited vibrations of non-shallow arches. Through laboratory experiments he verified theoretical results concerning regions of dynamic instability and magnitudes of vibration amplitudes. Among many convincing results he also reported an interesting experimental observation: "... with the approach to resonance, the picture of vibration is more complex and difficult to understand" [1, p. 331]. Bolotin hypothesized that these irregularities were consequences of non-idealities in the physical model not incorporated in the mathematical model. However, they might have been what is nowadays classified as "deterministic chaos". This is the hypothesis to be tested in the present study.

Non-linearities may cause mechanical systems to respond in a random-like manner to periodic excitation. The behaviour of the system is then extremely sensitive to initial conditions, precluding all but statistical long-term prediction even for strongly deterministic input and exact mathematical modelling. Such chaotic phenomena are presently studied intensively, by new mathematical tools, numerical simulations and laboratory experiments [2]. It has become increasingly clear that probably any strong non-linearity will cause even simple low-dimensional systems to behave chaotically for sufficiently strong forcing. Mechanical examples include driven pendulums [3, 4], impacting pendulums [5], magnetically buckled beams [6, 7], beams with stops [8], pin-jointed space trusses [9], elastic–plastic beams [10], fluid-conveying pipes [11], cylindrical shells [12], plates subject to fluid flow [13] and shallow arches [14].

The present study adds to this list a structure often encountered in engineering practice, the hinged–hinged non-shallow arch loaded at its crown by a vertical harmonic force (see Figure 1). The fundamental mode of vibration of this structure is antisymmetric, while the second mode is symmetric. For a wide range of opening angles 2α, the natural frequency ω_s of the second mode is approximately twice the natural frequency ω_a of the first mode. Thus, the non-shallow arch possesses a natural example of the so-called autoparametric
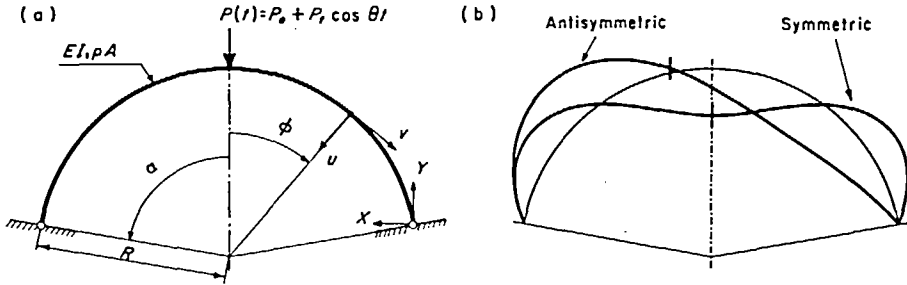
239

Figure 1. The double-hinged crown-loaded arch. (a) Geometry and loading; (b) fundamental vibration modes.

case of nearly commensurable linear natural frequencies, treated in particular by Nayfeh and co-workers (see, e.g., reference [15]). Besides becoming unstable through parametric excitation of the fundamental mode, when the excitation frequency $\theta \sim 2\omega_a$, the fundamental mode will also become unstable for $\theta \sim \omega_s$, through a non-linear modal interaction between the two modes. That is, when $\theta \sim \omega_s$, energy is initially pumped into the second mode until a saturation threshold is reached, beyond which additional energy spills over into the first mode. Compared to the classical single-mode parametrical excitation, where $\omega_s \gg \omega_a$ is assumed, the primary region of dynamic instability is significantly lowered and broadened, so that instabilities occur for lower forcing and for a wider range of excitation frequencies. Thus, autoparametric systems give rise to interesting physical behaviour, but also to real structures which may act dangerously to small periodic excitations.

The complicated behaviour of the relative simple system studied here is interesting simply for phenomenological reasons. However, the results also have practical implications. In the classical approach of the linear theory of dynamic stability, the ultimate goal is to locate the regions of dynamic instability in parameter space. According to linear theory, representative points inside the regions of instability correspond to exponentially growing amplitudes of the modelled physical system. Consequently, real structures are conservatively designed to operate well outside such regions. However, in reality amplitudes do not grow infinitely. At a certain level they become limited by various non-linearities, resulting in periodic, quasi-periodic or chaotic oscillations. The future states of a system in periodic or quasi-periodic motion is accurately predictable. If amplitudes associated with such motions become intolerable, it is possible to control them effectively by predictive structural control [16]. On the other hand, chaotic motion, is predictable only for very short time horizons ahead, and accordingly is much harder to control. Thus, it becomes increasingly important to single out subregions of the regions of dynamic instability corresponding to chaotic motion, if any.

In what follows, the arch model of Bolotin [1] is first summarized and non-dimensionalized. In section 3 the basic characteristics of the model are examined, and the stability of periodic solutions is determined by perturbation analysis. Finally, section 4 deals with non-periodic chaotic solutions.

2. EQUATIONS OF MOTION

2.1. THE LINEAR PROBLEM

Consider a double-hinged circular arch of radius R and opening angle 2α, loaded at the crown by a time-harmonic force $P(t)$ (see Figure 1). With the effects of shear and rotary

inertia neglected, the undamped forced in-plane vibrations are governed by [17, section 2.10]

$$\frac{EI}{R^4}\left[\frac{\partial^5 u}{\partial \phi^5} + 2\frac{\partial^3 u}{\partial \phi^3} + \frac{\partial u}{\partial \phi}\right] + \rho A\left[\frac{\partial}{\partial \phi}\left(\frac{\partial^2 u}{\partial t^2}\right) - \frac{\partial^2 v}{\partial t^2}\right] = \frac{\partial \Delta q_u}{\partial \phi} - \Delta q_v, \tag{1}$$

where $u = u(\phi, t)$ and $v = v(\phi, t)$ are the radial and tangential displacement components of the arch axis, ϕ is the angle measured from the axis of symmetry and EI and ρA are the constants of stiffness and mass per unit length respectively. The first term of equation (1) represents the internal tangential forces formed during bending of the arch axis, while the second term represents inertial forces. The right side represents additional forces which arise during buckling. If it is assumed that the loss of dynamic stability originates from the undeformed condition of the arch, this term is given by [1, section 80]

$$\frac{\partial \Delta q_u}{\partial \phi} - \Delta q_v = \begin{cases} -\dfrac{P}{2R}\left[\dfrac{\partial^2 \psi}{\partial \phi^2}(\sin \phi + \lambda \cos \phi) + 2\dfrac{\partial \psi}{\partial \phi}(\cos \phi - \mu \sin \phi)\right], & \phi > 0 \\[2mm] -\dfrac{P}{2R}\left[\dfrac{\partial^2 \psi}{\partial \phi^2}(\lambda \cos \phi - \sin \phi) - 2\dfrac{\partial \psi}{\partial \phi}(\cos \phi + \mu \sin \phi)\right], & \phi < 0 \end{cases}, \tag{2}$$

where ψ is the increment of cross-sectional rotation,

$$\psi(\phi, t) = (1/R)(\partial u/\partial \phi + v), \tag{3}$$

and μ is defined through the Cartesian (X, Y) co-ordinates of the arch axis:

$$\mu = \int_0^\alpha XY \, d\phi \bigg/ \int_0^\alpha Y^2 \, d\phi = \frac{4\cos \alpha - 3\cos 2\alpha - 2\alpha \sin 2\alpha - 1}{4\alpha + 2\alpha \cos 2\alpha - 3\sin 2\alpha}. \tag{4}$$

Due to the non-rotating force $P(t)$, assumed for simplicity, expression (2) has an integrable discontinuity at $\phi = 0$:

$$\lim_{\varepsilon \to 0} \int_{-\varepsilon}^{+\varepsilon}\left(\frac{\partial \Delta q_u}{\partial \phi} - \Delta q_v\right) d\phi = -\frac{P}{R}\psi(0, t). \tag{5}$$

An approximate Galerkin solution of equation (1) will be sought for the common case of a non-shallow arch for which the fundamental antisymmetric mode of vibration is predominant. Assume that the axis of the arch is incompressible,

$$u(\phi, t) = \partial v(\phi, t)/\partial \phi, \tag{6}$$

and that

$$u(\phi, t) = \bar{f}(t)\sin(\pi\phi/\alpha), \qquad v(\phi, t) = -(\alpha/\pi)\bar{f}(t)(1 + \cos(\pi\phi/\alpha)), \tag{7a, b}$$

which is the lowest antisymmetric mode of free arch vibrations when tangential inertia is neglected, weighted by an unknown amplitude function $\bar{f}(t)$. Substitute these expressions into equation (1), multiply by $[1 + \cos(\pi\phi/\alpha)]$ and integrate between $\mp \alpha$ to obtain

$$d^2\bar{f}/dt^2 + \omega_a^2(1 - P(t)/P_*)\bar{f} = 0. \tag{8}$$

Here ω_a is the approximate fundamental frequency of free antisymmetric vibrations,

$$\omega_a = (\pi/2R)\sqrt{EI/M_0 R\alpha}\,((\pi/\alpha)^2 - 1), \qquad M_0 = \rho AR\alpha((\pi/2\alpha)^2 + \tfrac{3}{4}), \qquad (9)$$

where M_0 represents the lumping of all distributed mass at the crown, while P_* is the static buckling load,

$$P_* = [EI\alpha/R^2 H(\alpha)]((\pi/\alpha)^2 - 1)^2 \qquad (10)$$

in which

$$H(\alpha) = 1 - \cos\alpha - \mu\sin\alpha - 2\left(1 - \frac{2\alpha^2}{\pi^2}\right)$$

$$+ \frac{((2\pi^2/\alpha^2) + 1)((\pi^2/\alpha^2) - 1)}{(4\pi^2/\alpha^2) - 1}\,(1 - \cos\alpha + \mu\sin\alpha). \qquad (11)$$

Equation (8) describes the horizontal vibration amplitude of the arch crown when symmetric vibrations are negligible. For $P(t) = P_0 + P_t\cos\theta t$ it takes the form of the well-known Mathieu-Hill equation, with an unstable Arnold-tongue emanating from $\theta = 2\omega_a$ in the (θ, P_t) plane. Thus, for $\theta \approx 2\omega_a$ the symmetric force will excite unstable antisymmetric vibrations.

2.2. THE NON-LINEAR PROBLEM

In reality amplitudes do not grow unbounded when $\theta \sim 2\omega_a$, as predicted by the linear model (8). They become limited by non-linearities, arising primarily from second order vertical displacements of the crown due to antisymmetric vibrations. Furthermore, the amplitudes are affected by symmetric displacement components, which inevitably will accompany any symmetrical forcing. In the presence of small symmetric displacements, equation (8) must be altered so as to include the total force transmitted to the crown,

$$\frac{d^2\bar{f}}{dt^2} + \omega_a^2\left(1 - \frac{P(t) - M_0\,d^2\bar{w}/dt^2}{P_*}\right)\bar{f} = 0, \qquad (12)$$

where M_0 is the equivalent crown mass defined in equations (9), and $\bar{w}$ is the total vertical displacement of the crown,

$$\bar{w} = \bar{u} + \Delta\bar{u}_0, \qquad (13)$$

in which $\bar{u}$ denotes the symmetric displacement component at the crown, and $\Delta\bar{u}_0$ is the second order vertical displacement due to antisymmetric vibration. The latter can be calculated by a balance of energy [1, section 81],

$$\Delta\bar{u}_0 = [H(\alpha)/2R]\,\bar{f}^2, \qquad (14)$$

where $H(\alpha)$ is defined by equation (11). For small symmetric displacements, the total force transmitted to the arch is approximately governed by

$$P(t) - M_0\,d^2\bar{w}/dt^2 = k\bar{u}, \qquad (15)$$

where k is the symmetric stiffness of the arch. The equation governing antisymmetric vibrations is obtained by substituting expression (15) into equation (12),

$$\frac{d^2\bar{f}}{dt^2} + 2c_a\frac{d\bar{f}}{dt} + \omega_a^2\left(1 - \frac{M_0\omega_s^2}{P_*}\bar{u}\right)\bar{f} = 0, \qquad (16)$$

in which a viscous damping term has been added, and

$$\omega_s^2 = k/M_0 \qquad (17)$$

denotes the natural frequency of linear symmetric vibrations. The equation governing symmetric vibrations is obtained by substituting equations (13), (14), (17) and $P(t) = P_0 + P_t \cos \theta t$ into equation (15),

$$\frac{d^2 \bar{u}}{dt^2} + 2c_s \frac{d\bar{u}}{dt} + \omega_s^2 \bar{u} + \frac{H(\alpha)}{R} \left[\bar{f} \frac{d^2 \bar{f}}{dt^2} + \left(\frac{d\bar{f}}{dt} \right)^2 \right] = \frac{P_0 + P_t \cos \theta t}{M_0}, \qquad (18)$$

to which viscous damping also has been added.

Equations (16) and (18) are non-dimensionalized by expressing time and frequencies in terms of the statically loaded natural frequency $\tilde{\omega}_a$ of the fundamental mode,

$$\tilde{\omega}_a = \omega_a \sqrt{1 - P_0/P_*}, \qquad (19)$$

which, rather than ω_a, constitutes the quantity typically measured in experiments. The non-dimensional system becomes

$$\ddot{f} + 2\beta \dot{f} + (1 - m\omega^2 u)f = 0, \qquad \ddot{u} + 2\beta \omega \dot{u} + \omega^2 u + \kappa(f\ddot{f} + \dot{f}^2) = (q/m) \cos \Omega \tau, \qquad (20a, b)$$

where $(\dot{\ }) = d(\ )/d\tau$ and the non-dimensional groups are defined as follows:

time: $\tau = \tilde{\omega}_a t$;   displacements: $f = \bar{f}/R$, $u = (\bar{u} - P_0/(M_0\omega_s^2))/R$;

frequencies: $\Omega = \theta/\tilde{\omega}_a$, $\omega = \omega_s/\tilde{\omega}_a$;   damping: $\beta = c_a/\tilde{\omega}_a = c_s/\omega_s$;

load: $q = P_t/(P_* - P_0)$;

non-linearities: $\kappa = H(\alpha)$, $m = M_0 R \tilde{\omega}_a^2/(P_* - P_0) = (\pi/2\alpha) H(\alpha)$. $\qquad (21)$

Note that the non-dimensional symmetric displacement u refers to the statically deformed position of the crown, that Ω denotes the excitation frequency in proportion to the fundamental linear natural frequency while ω expresses the separation between symmetric and antisymmetric natural frequencies, that the damping is expressed as a fraction of the critical, and that q measures the dynamic component of the load as a fraction of the buckling load which remains when the static load P_0 is applied. Note also that the non-linearities m and κ cannot be chosen independently, as they are determined solely by the opening angle 2α of the arch.

3. THEORETICAL ANALYSIS OF PERIODIC MOTION

3.1. THE ZERO-SOLUTION

An approximation to the boundaries of dynamic stability of the linear solution $f = 0$ is obtained by neglecting the nonlinearity of equation (20b), whereby the symmetric vibration component is given by

$$u_0 = A_0(q/m\omega^2) \cos (\Omega \tau - \theta_0), \qquad (22)$$

where

$$A_0 = [(1 - (\Omega/\omega)^2)^2 + (2\beta\Omega/\omega)^2]^{-1/2}, \qquad \tan \theta_0 = 2\beta\omega\Omega/(\omega^2 - \Omega^2). \qquad (23)$$

Substituting u_0 for u in equation (20a) yields, for antisymmetric vibrations,

$$\ddot{f} + 2\beta\dot{f} + [1 - qA_0 \cos (\Omega \tau - \theta_0)]f = 0, \qquad (24)$$

which can be transformed into the standard Mathieu–Hill equation:

$$\frac{d^2 f}{d\tilde{\tau}^2} + 2\tilde{\beta}\frac{df}{d\tilde{\tau}} + (\tilde{\omega} + 2\tilde{q}\cos 2\tilde{\tau})f = 0 \tag{25}$$

through the substitutions

$$2\tilde{\tau} = \Omega\tau - \theta_0, \qquad \tilde{\beta} = 2\beta/\Omega, \qquad \tilde{\omega} = 4/\Omega^2, \qquad \tilde{q} = -2qA_0/\Omega^2. \tag{26}$$

A second order approximation to the principal boundary of dynamic instability of equation (25) is given by [18, section 5.3.5]

$$\tilde{\omega}_* = 1 \pm \sqrt{\tilde{q}^2 - 4\tilde{\beta}^2} - \tfrac{1}{8}\tilde{q}^2, \tag{27}$$

or, in terms of the original variables,

$$q_* = \Omega\sqrt{2[(1 - (\Omega/\omega)^2)^2 + (2\beta\Omega/\omega)^2][5\Omega^2 - 4 - 2\Omega\sqrt{6\Omega^2 - 8 - 4\beta^2}]}. \tag{28}$$

The instability boundaries given by equation (28) are shown in Figure 2 for small damping. On the boundary curves the solutions of equation (25) are periodic with twice the forcing period. Inside the hatched regions the zero solution is unstable, and linear theory predicts that antisymmetric vibrations will grow exponentially. Outside the unstable regions, small initial perturbations will decay to zero, and the zero solution is asymptotically stable. For $\omega \gg 2$ (see Figure 2(a)) there are two distinct regions of dynamic instability, the first around $\Omega = 2$, corresponding to a forcing frequency twice as large as the fundamental antisymmetric natural frequency, the second around $\Omega = \omega$, corresponding to resonant excitation of the first symmetric mode of the arch. As $\omega \to 2$ (see Figure 2(b)) these two regions merge into one, and approach the $q = 0$ axis. This so-called autoparametric case is particularly dangerous because unstable vibrations may be excited by extremely small loads of a rather wide frequency band.
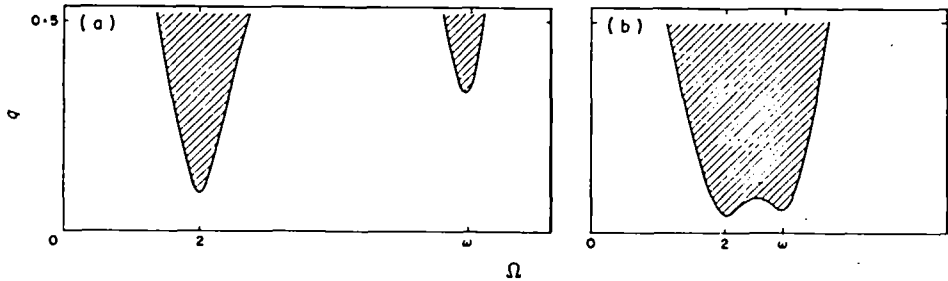

Figure 2. Primary region of dynamic instability (hatched). q, Excitation magnitude; Ω, excitation frequency. (a) $\omega \gg 2$, resonance frequency of symmetric vibrations far from twice the resonance of antisymmetric vibrations; (b) $\omega \approx 2$, almost internal resonance (the autoparametric case).

3.2. PERIODIC SOLUTIONS

Periodic solutions of the model equations (20) are sought by non-linear perturbation analysis. Nayfeh and co-workers [15, 19] used the method of multiple scales to study the solutions of general two-degree-of-freedom systems with quadratic non-linearities, of which equation (20) is a special case. It was shown that solutions near and inside the primary region of dynamic instability are dominated by the primary resonance $\Omega = \omega$, and the internal resonance $\omega = 2$. The results of Nayfeh are readily applicable here. However, instead of perturbing around the primary resonance $\Omega = \omega$ for weak excitation, as was done in reference [15], we shall here perturbate around the secondary resonance $\Omega = 2$ for

hard excitations. To indicate the smallness of damping and non-linearities we introduce a small parameter ε into equations (20), which in the final equations is set to unity:

$$\ddot{f} + \varepsilon 2\beta \dot{f} + (1 - \varepsilon m\omega^2 u)f = 0, \qquad \ddot{u} + \varepsilon 2\beta\omega\dot{u} + \omega^2 u + \varepsilon\kappa(f\ddot{f} + \dot{f}^2) = (q/m)\cos\Omega\tau. \quad (29a, b)$$

Following the method of multiple scales [18] the solutions of equations (29) are approximated by uniformly valid expansions,

$$f = f_0(T_0, T_1) + \varepsilon f_1(T_0, T_1) + \cdots, \qquad u = u_0(T_0, T_1) + \varepsilon u_1(T_0, T_1) + \cdots, \quad (30a, b)$$

where $f_{0,1}$ and $u_{0,1}$ are functions to be determined, $T_0 = \tau$ is a fast scale characterizing motions at the frequencies 1, 2, ω and Ω, while $T_1 = \varepsilon\tau$ is a slow scale characterizing modulations of amplitudes and phases. Substituting equations (30) into equations (29) and equating like powers of ε gives, to order ε^0,

$$D_0^2 f_0 + f_0 = 0, \qquad D_0^2 u_0 + \omega^2 u_0 = (q/m)\cos\Omega T_0 \qquad (31a, b)$$

and, to order ε^1,

$$D_0^2 f_1 + f_1 = -2D_0 D_1 f_0 - 2\beta D_0 f_0 + m\omega^2 u_0 f_0, \qquad (32a)$$

$$D_0^2 u_1 + \omega^2 u_1 = -2D_0 D_1 u_0 - 2\beta\omega D_0 u_0 - \kappa[f_0 D_0^2 f_0 + (D_0 f_0)^2], \qquad (32b)$$

where the operator $D_{0,1} = \partial/\partial T_{0,1}$. The solution of the first order problem (31) is conveniently expressed in complex notation as

$$f_0 = A_1(T_1)\, e^{iT_0} + \bar{A}_1(T_1)\, e^{-iT_0}, \qquad (33a)$$

$$u_0 = A_2^\ast(T_1)\, e^{i\omega T_0} + \bar{A}_2^\ast(T_1)\, e^{-i\omega T_0} + [\tfrac{1}{2}q^\ast/(\omega - \Omega)](e^{i\Omega T_0} + e^{-i\Omega T_0}), \qquad (33b)$$

where A_1 and $A_2^\ast$ are yet unknown complex functions of T_1, bars denote complex conjugation and $q^\ast$ is defined by

$$q^\ast = (q/m)/(\omega + \Omega). \qquad (34)$$

Substituting equations (33) into the second order problem (32) yields

$$D_0^2 f_1 + f_1 = -i2(A_1' + \beta A_1)\, e^{iT_0} - 4\Lambda_1(A_1 A_2^\ast\, e^{i(\omega + 1)T_0} + \bar{A}_1 A_2^\ast\, e^{i(\omega - 1)T_0})$$
$$\qquad -2\Lambda_1[q^\ast/(\omega - \Omega)](A_1\, e^{i(\Omega + 1)T_0} + \bar{A}_1\, e^{i(\Omega - 1)T_0}) + c.c., \qquad (35a)$$

$$D_0^2 u_1 + \omega^2 u_1 = -i2\omega(A_2^{\ast\prime} + \beta\omega A_2^\ast)\, e^{i\omega T_0} - i\beta\Omega\omega[q^\ast/(\omega - \Omega)]\, e^{i\Omega T_0} - 4\omega\Lambda_2 A_1^2\, e^{i2T_0} + c.c., \qquad (35b)$$

where $i = \sqrt{-1}$, $(\;)' = d/dT_1$, c.c. denotes terms which are complex conjugates of the preceding terms, and $\Lambda_{1,2}$ defines the non-linearities:

$$\Lambda_1 = -\tfrac{1}{4}m\omega^2, \qquad \Lambda_2 = -\tfrac{1}{2}\kappa/\omega. \qquad (36)$$

The functions A_1 and $A_2^\ast$ are determined by the requirement that solutions to (35a, b) do not contain secular terms, or small-divisor terms caused by resonance. The resonant conditions are $\omega = 2$ (internal resonance), $\Omega = \omega$ (primary resonance of second mode) and $\Omega = 2$ (secondary resonance of the first mode). The nearness to internal resonance and secondary resonance is expressed by detuning parameters σ_1 and σ_2:

$$\omega = 2 + \varepsilon\sigma_1 \quad (\Rightarrow \omega T_0 = 2T_0 + \sigma_1 T_1), \qquad \Omega = 2 + \varepsilon\sigma_2 \quad (\Rightarrow \Omega T_0 = 2T_0 + \sigma_2 T_1). \quad (37a, b)$$

When expressions (37) are inserted into equations (35), small-divisor terms convert into secular terms. Eliminating terms producing secular terms in f_1 and u_1 gives the solvability conditions:

$$i2(A_1' + \beta A_1) + 4\Lambda_1\bar{A}_1 A_2\, e^{i\sigma_2 T_1} = 0, \tag{38a}$$

$$i2[A_2' + \{\beta\omega - i(\sigma_1 - \sigma_2)\}A_2] + 4\Lambda_2 A_1^2\, e^{-i\sigma_2 T_1} - (1 + i\beta)(\sigma_1 - \sigma_2)q^* = 0, \tag{38b}$$

where the definition of a new function A_2,

$$A_2(T_1) = A_2^*(T_1)\, e^{i(\sigma_1 - \sigma_2)T_1} + [\tfrac{1}{2}q^*/(\omega - \Omega)], \tag{39}$$

greatly simplifies the results to follow. It is convenient to express the complex functions $A_{1,2}$ in the forms

$$A_1 = \tfrac{1}{2}a_1\, e^{ib_1}, \qquad A_2 = \tfrac{1}{2}a_2\, e^{ib_2}, \tag{40}$$

where $a_{1,2}$ and $b_{1,2}$ are real functions of T_1. Substituting expressions (40) into equations (38) gives, when real and imaginary parts are separated, the equations governing amplitude and phase modulations:

$$a_1' = -\beta a_1 - \Lambda_1 a_1 a_2 \sin(\gamma_1 + \gamma_2), \tag{41a}$$

$$a_2' = -\beta\omega a_2 + \Lambda_2 a_1^2 \sin(\gamma_1 + \gamma_2) + q^*(\beta \cos\gamma_2 - \sin\gamma_2), \tag{41b}$$

$$a_1\gamma_1' = \sigma_2 a_1 - 2\Lambda_1 a_1 a_2 \cos(\gamma_1 + \gamma_2), \tag{41c}$$

$$a_2\gamma_2' = (\sigma_1 - \sigma_2)a_2 + \Lambda_2 a_1^2 \cos(\gamma_1 + \gamma_2) - q^*(\cos\gamma_2 + \beta\sin\gamma_2). \tag{41d}$$

Here

$$\gamma_1 = \sigma_2 T_1 - 2b_1 \quad \text{and} \quad \gamma_2 = b_2. \tag{42}$$

The system response is found by substituting equations (33), (40), (42), (37), (39) and $T_0 = \tau$, $T_1 = \varepsilon\tau$ into equations (30), giving

$$f = a_1 \cos(\tfrac{1}{2}\Omega\tau - \tfrac{1}{2}\gamma_1) + [2\Lambda_1 a_1 a_2 / \{(\tfrac{3}{2}\Omega)^2 - 1\}] \cos(\tfrac{3}{2}\Omega\tau - \tfrac{1}{2}\gamma_1 + \gamma_2) + O(\varepsilon^2), \tag{43a}$$

$$u = a_2 \cos(\Omega\tau + \gamma_2) + O(\varepsilon^2), \tag{43b}$$

where the second order terms are given as the solutions of equations (35), and where $a_{1,2}$ and $\gamma_{1,2}$ are unknown modulation functions in the slow scale T_1. It is seen that for $a_1 \neq 0$ and constant phasing $\gamma_{1,2}$ the antisymmetric mode becomes locked at half the excitation frequency (and higher harmonics hereof).

Periodic solutions of the system correspond to constant values of amplitudes $a_{1,2}$ and phases $\gamma_{1,2}$: i.e., to fixed points of the modulation equations (41). By setting $a_1' = a_2' = \gamma_1' = \gamma_2' = 0$ in equations (41) it is found that there are two possibilities. Either

$$a_1 = a_{1l} = 0 \quad \text{and} \quad a_2^2 = a_{2l}^2 = q^{*2}(1 + \beta^2)/[(\sigma_1 - \sigma_2)^2 + \beta^2\omega^2], \tag{44}$$

which is essentially the linear solution (corresponding to pure symmetric vibrations of the arch), or

$$a_1^2 = a_{1n}^2 = (1/\Lambda_1\Lambda_2)(\chi_1 \pm \sqrt{\Lambda_1^2 g^2 - \chi_2^2}) \quad \text{and} \quad a_2^2 = a_{2n}^2 = (\tfrac{1}{4}\sigma_2^2 + \beta^2)/\Lambda_1^2, \tag{45}$$

where

$$\chi_1 = -\tfrac{1}{2}\sigma_2(\sigma_1 - \sigma_2) - \beta^2\omega, \qquad \chi_2 = (\sigma_1 - \sigma_2)\beta - \tfrac{1}{2}\beta\omega\sigma_2 \quad \text{and} \quad g = q^*\sqrt{1 + \beta^2}, \tag{46, 47}$$

which constitutes the non-linear solutions characterized by modal interaction.

The stability of periodic solutions are governed by the eigenvalues of the Jacobian of equations (41), evaluated at the fixed points. A particular fixed point is unstable if at least one eigenvalue has a positive real part. It is found that the linear solution (44) is unstable if, and only if, $a_{2l}^2 > a_{2n}^2$; otherwise it is stable. By examining the stability of the non-linear solutions (45) it is found that the characteristic polynomial in the eigenvalues z is

$$z^4 + r_1 z^3 + r_2 z^3 + r_4 = 0, \qquad (48)$$

where

$$r_1 = 2\beta(\omega + 1), \qquad r_2 = 4\Lambda_1\Lambda_2 a_{1n}^2 + \beta^2\omega^2 + 4\beta^2\omega + (\sigma_1 - \sigma_2)^2,$$

$$r_3 = 4\Lambda_1\Lambda_2 a_{1n}^2 \beta(\omega + 1) + 2\beta^3\omega^2 + 2\beta(\sigma_1 - \sigma_2)^2, \qquad (49)$$

$$r_4 = 4\Lambda_1\Lambda_2 a_{1n}^2 [\Lambda_1\Lambda_2 a_{1n}^2 + \beta^2\omega + \tfrac{1}{2}\sigma_2(\sigma_1 - \sigma_2)].$$

According to the Routh–Hurwitz criterion, at least one root of equation (48) has a positive real part if and only if

$$r_4 < 0 \qquad \text{or} \qquad r_1 r_2 - r_3 < 0 \qquad \text{or} \qquad r_3(r_1 r_2 - r_3) - r_1^2 r_4 < 0. \qquad (50)$$

Consequently, if conditon (50) is satisfied the non-linear solution is unstable; otherwise it is stable.

The model behaviour inside the around the primary region of dynamic instability is visualized in Figures 3, 4 and 5 for parameters $\omega = 2.44$, $\kappa = 2.63$, $m = 3.32$ and $\beta = 0.03$, corresponding to a weakly damped arch of opening span 160°.
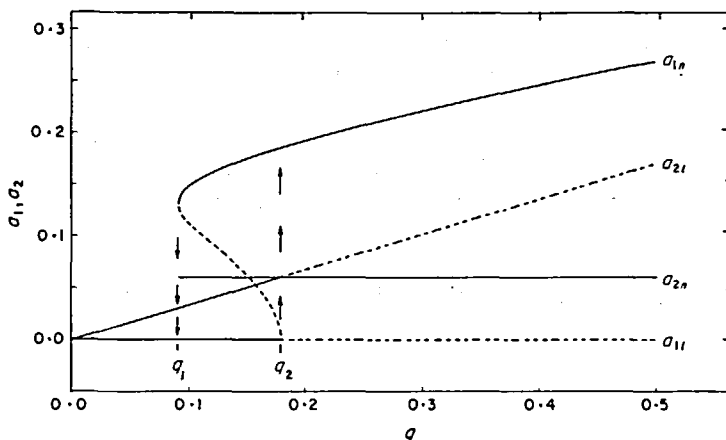

Figure 3. Variation of steady state modal amplitudes a_1 and a_2 with excitation amplitude q. ——, Stable; – – – –, unstable; l, linear; n, non-linear. ($\Omega = 2.6$, $\omega = 2.44$, $\kappa = 2.63$, $m = 3.32$, $\beta = 0.03$.).

In Figure 3 is shown the variation of steady state modal amplitudes $a_{1,2}$ with excitation amplitude q, when the excitation frequency $\Omega = 2.6$. Unstable solutions are represented by dashed lines. Four non-linear features appear: (1) there are *jumps* in the response when the load is increased beyond $q = q_2$ and a_1 is on the linear branch a_{1l}, or when q is decreased below $q = q_1$ and a_1 is on the non-linear branch a_{1n}; (2) the amplitude of the second mode a_2 becomes *saturated* as q is increased beyond $q = q_2$, and additional energy spills over into the first mode, raising only the magnitude of a_1; (3) there are *shifts* in the number of *fixed points* (one stable for $q < q_1$, one stable and one unstable for $q > q_2$, and two stable and one unstable for $q_1 < q < q_2$); (4) between the bifurcation points q_1 and q_2 the stationary solution actually obtained is dependent on the initial conditions.
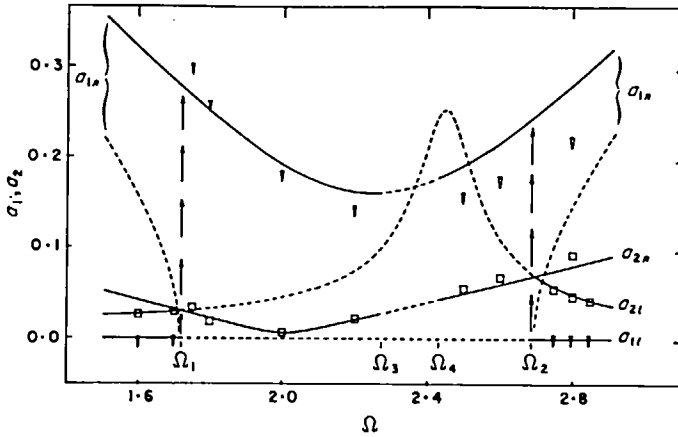
Figure 4. Variation of modal amplitudes a_1 and a_2 with excitation frequency Ω. ———, Stable; - - - - -, unstable; l, linear; n, non-linear; $\square$, ∇, numerical simulation.

In Figure 4 is shown the variation of modal amplitudes $a_{1,2}$ with excitation frequency Ω when the excitation amplitude $q = 0 \cdot 3$. It appears that when Ω is increased beyond Ω_1, or decreased below Ω_2, the linear branches become unstable and the solution jumps to the non-linear branches. Furthermore, in the frequency range $\Omega_3 < \Omega < \Omega_4$ neither expression (44) nor expression (45) are stable solutions. At the critical frequencies $\Omega_{3,4}$ the real part of a pair of complex conjugate eigenvalues crosses the imaginary axis, giving rise to a Hopf bifurcation and limit cycle behaviour of $a_{1,2}$. These solutions are studied further in section 4. Note, also, that the non-linear modal interaction leads to a significant reduction in the amplitude of the second mode a_2, even at primary resonance $\Omega = \omega = 2 \cdot 44$. In Figure 4 the results are also shown of numerical integration of the model equations (20), which in view of the relative hard excitation match the theoretical results very well. The largest discrepancies are associated with the non-linear upper branch of a_1, for which the second term of equation (43a) cannot be neglected. (The magnitude of this term is 12% of a_1 at $\Omega = 1 \cdot 5$, and 5% of a_1 at $\Omega = 2 \cdot 9$.)

In Figure 5 are shown the stability boundaries separating qualitatively different behaviours of the system in the space of the excitation frequency Ω and magnitude q. In the
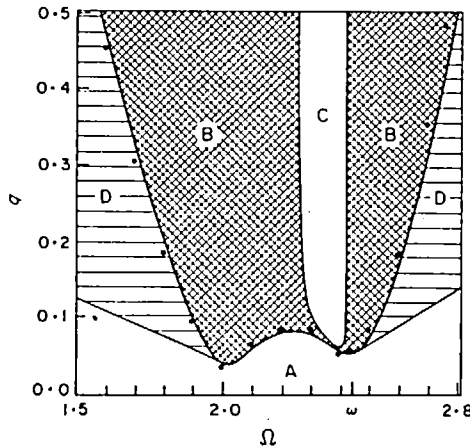

Figure 5. Boundaries of dynamic instability. Ω, q, Excitation frequency and magnitude. Region A, only stable solution is equation (44); region B, only stable solution is equation (45); region C, neither solution stable; region D, both solutions stable; ●, numerical simulation.

region A only the linear solution (44) of pure symmetric vibrations ($a_1 = 0$) is stable, while in region B only the non-linear solution (45) involving modal interaction ($a_1 \neq 0$) is stable. In region C neither of these solutions are stable, while in region D both are stable.

The curve separating regions B and D constitutes the classical boundary of dynamic instability (compare it with Figure 2(b)). Although it was obtained by using first order perturbation theory, it is almost indistinguishable from that obtained when using the second order Mathieu–Hill solution (28). As appears from the figure, it also matches the boundary obtained by numerical simulations of the model equations (20) very well.

The results given above are similar to those presented by Nayfeh [15] for $q \approx O(\varepsilon)$ and $\Omega \approx \omega$. In fact it is found that the results of reference [15] are exactly obtained as $\omega \rightarrow \Omega$ in equation (34), and the (small) β^2-term of equation (47) is neglected. The consequence, however, is that the instability boundary between regions B and D in Figure 5 tilts to the right, away from the results obtained when using both Mathieu–Hill theory and numerical simulations.

4. NUMERICAL ANALYSIS OF NON-PERIODIC MOTION

In this section the extremely rich behaviour of the system is first exemplified for a few values of excitation frequency and magnitude (Ω, q). Then bifurcations along a line of constant q are studied. Finally, the chaotic subregions of the primary region of dynamic instability are located.

The model equations (20) were rewritten as a system of first order equations. These were solved numerically by using fifth and sixth order Runge–Kutta integration and, for comparison, Adams' Predictor Corrector Method. In all cases $\beta = 0.03$ and $\omega = 2.44$, $\kappa = 2.63$, $m = 3.32$, corresponding to weakly damped arches of opening span $160°$. Unless explicitly stated initial conditions were $(f_0, \dot{f}_0, u_0, \dot{u}_0) = (0.13, 0, 0.01, 0)$. Only post-transient motion was considered, requiring typically 100–4000 forcing periods to pass without data-sampling.

Some characteristics of the motion for different Ω when $q = 0.2$ are shown in Figure 6. The Poincaré sections given were obtained by sampling the $(f, \dot{f})$-state at discrete post-transient times $\tau_n = 2\pi n/\Omega$, $n = 1, 2, \ldots$; i.e., once per forcing period. The largest Lyapunov exponent λ_1 also given is defined as $\lambda_1 = \max(\lambda_i)$, $i = 1, n$ where n is the dimension of the system, and [20]

$$\lambda_i = \lim_{\tau \to \infty} [(1/\tau) \log_2 \{r_i(\tau)/r_i(0)\}], \tag{51}$$

where $r_i(\tau)$ measures the growth of an infinitesimal n-sphere of initial conditions at $\tau = 0$ in terms of the ith ellipsoidal principal axis. (The zero exponent corresponding to the time dimension is not considered.) Lyapunov exponents essentially measure the average rates of convergence or divergence of nearby orbits in phase space. $\lambda_1 > 0$ indicates an exponential separation of nearby orbits, a stretch of the phase space. In real systems the phase space is always bounded, giving rise to back-foldings of escalating orbits. This process of stretching a folding is what defines chaos.

At $\Omega = 2.25$ (see Figure 6(a)) the motion of the antisymmetric displacement component f is periodic, yielding a closed curve in phase space. The Poincaré section consists of two points, implying a period-2 motion at half the excitation frequency. This also appears from the spike at $\omega^* = \frac{1}{2}\Omega$ in the power spectrum, which has an additional component at $\frac{3}{2}\Omega$ in accordance with the theoretical result (43a).

At $\Omega = 2.295$ (see Figure 6(b)) the Hopf bifurcation curve separating regions B and C of Figure 5 has been crossed. The period of the f-component has doubled four times,
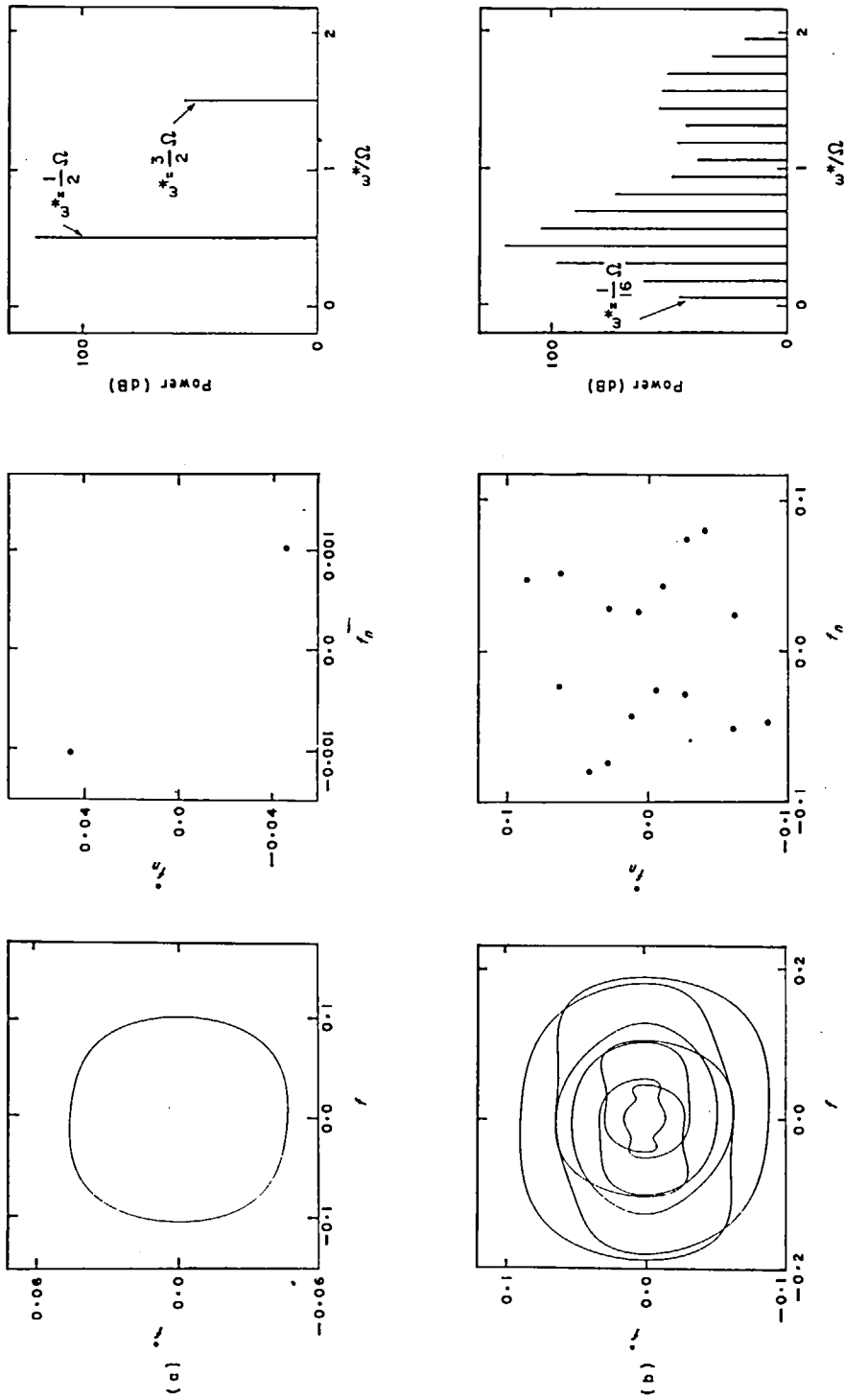
Figure 6. Post-transient phase plane trajectories (left), Poincaré sections (middle) and power spectra (right) of the antisymmetric vibration amplitude f, for constant load $q = 0.2$ and increasing excitation frequency Ω. ($\omega = 2.44$, $\beta = 0.03$, $m = 3.32$, $\kappa = 2.63$.) (a) $\Omega = 2.25$, period-2, $\lambda_1 = 0.007$; (b) $\Omega = 2.295$, period-16, $\lambda_1 = -0.03$; (c) $\Omega = 2.318$, quasi-periodic, $\lambda_1 = 0$; (d) $\Omega = 2.4$, chaotic, $\lambda_1 = +0.026$.
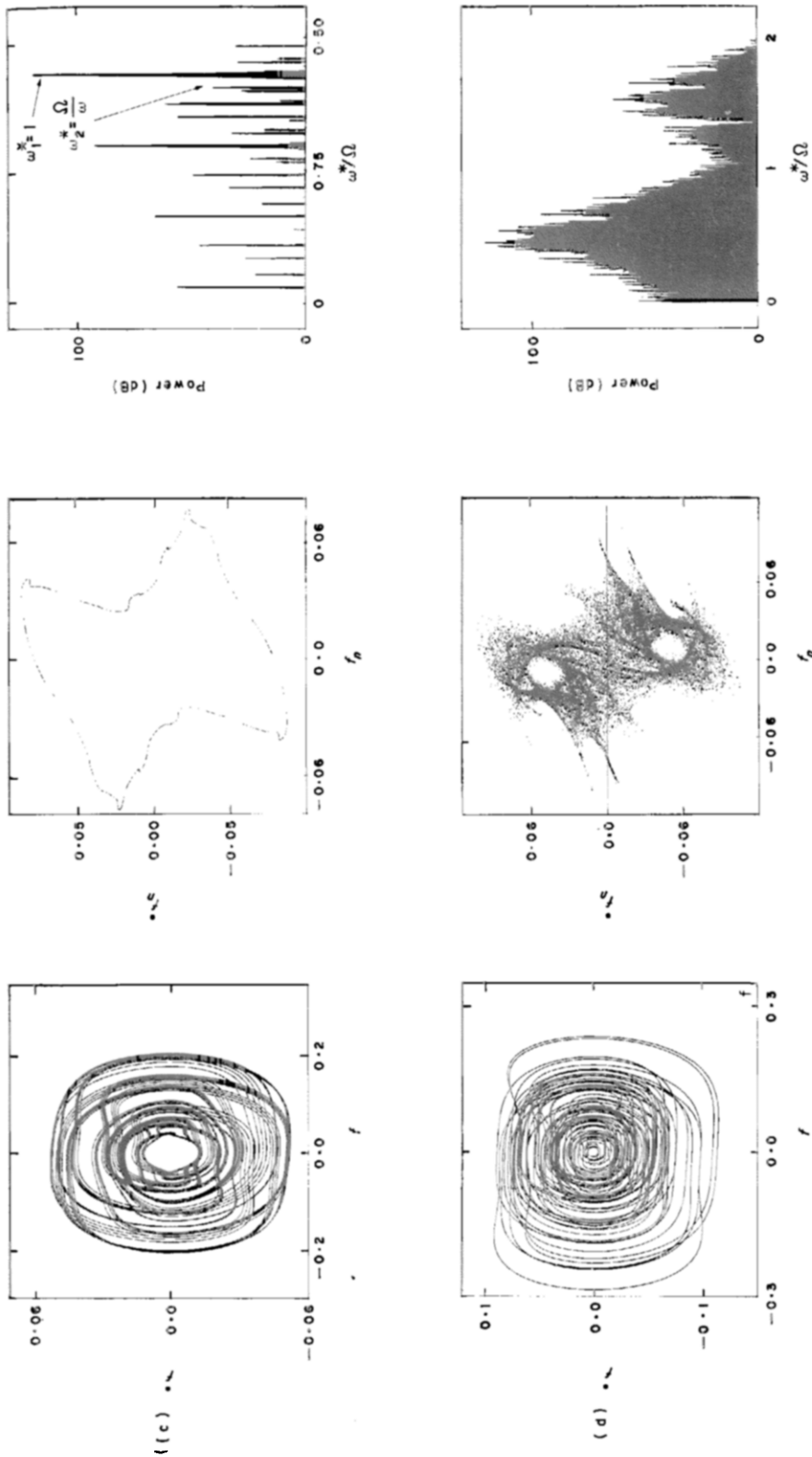
Figure 6—continued.

resulting in period-16 motion with subharmonics at $(k/2^4)\Omega$, $k = 1, 3, 5, \ldots, 15$, together with higher harmonics. As for Figure 6(a) the largest Lyapunov exponent is negative, implying that orbits nearly converge and the motion is accurately predictable at all future time instances.

At $\Omega = 2\cdot318$ (see Figure 6(c)) orbits fill the phase plane in a seemingly complicated pattern. The Poincaré section shows that the attracting set is a closed curve (in fact a section of a torus) indicating quasi-periodic motion at two or more incommensurate frequencies. This is confirmed by the discrete power spectrum, with spikes at the two (almost) incommensurable frequencies 1 and Ω/ω together with subharmonics $k/2^4$, $(k/2^4)(\Omega/\omega)$, $k = 1, 2, \ldots, 15$, and higher harmonics thereof. (Note that $\omega^* = 1$ corresponds to oscillations at the antisymmetric natural frequency of the arch, certainly not a trivial stationary response far beyond primary resonance of this mode.) The largest Lyapunov exponent becomes zero, implying that initially close orbits stay close and that future motion is predictable.

At $\Omega = 2\cdot4$ (see Figure 6(d)) the motion becomes chaotic. Orbits fill out the phase plane, broadband noise enters the power spectrum, and the Poincaré section indicates a strange attractor of fractal dimension. λ_1 takes on the positive value $0\cdot026$ bits/second, implying that infinitesimally close orbits diverge exponentially with time. In fact, if an initial point were specified with an accuracy of one part per million (20 bits), all information about the state would be lost after $20/0\cdot026 = 769$ seconds, corresponding to 294 forcing periods, except that the point would be somewhere on the attractor. The full spectrum of Lyapunov exponents λ_i, $i = 1, 5$ (including the time dimension) were computed by using the method of Wolf et al. [20] to $(+0\cdot026, 0, -0\cdot0038, -0\cdot064, -0\cdot083)$. Thus, there is only one positive exponent, and the sum of all exponents is negative in accordance with the contracting nature of the dissipative phase space. The Lyapunov dimension [20]

$$d_L = j + \sum_{i=1}^{j} \lambda_i / |\lambda_{j+1}|, \quad \text{where } \sum_{i=1}^{j} \lambda_i > 0 \text{ and } \sum_{i=1}^{j+1} \lambda_i < 0, \quad (52)$$

is in this case $3\cdot35$, implying that the dynamics of the system cannot be captured with substantially fewer variables than the five already used $(f, \dot{f}, u, \dot{u}, \tau)$.

The system response to continuously changing load parameters (Ω, q) was studied through numerical bifurcation maps. In Figure 7 is shown the value of the antisymmetric amplitude f at discrete times τ_n, 270° out of phase with the driving force, when $q = 0\cdot2$ and Ω is varied through the primary region of dynamic instability. The Ω-range was sampled at 300 discrete points. For each of these, 4000 periods of the driving force were discarded as transients before the next 300 values of f_n were plotted.

In Figure 7(a), $\Omega_{1,2,3,4}$ denote the theoretically computed frequencies separating the regions B, C and D of Figure 5. In the ranges $\Omega_1 - \Omega_3$ and $\Omega_4 - \Omega_2$ only the non-linear period-2 motion should be stable, while between Ω_3 and Ω_4 all theoretical perturbation solutions were unstable. As appears from the figure, this was roughly confirmed by the numerical simulations (Ω_4 seems to be slightly underestimated). Beyond Ω_1 only the period-2 solution is stable, until the Hopf bifurcation occurs at Ω_3. Beyond Ω_3 the response is quasi-periodic with periodic windows (the largest Lyapunov exponent λ_1 being zero or negative), until the system turns chaotic at Ω_5 where $\lambda_1 > 0$. Slightly above Ω_4 chaos disappears, and period-2 cycles reenter until the zero-solution becomes stable at Ω_2.

The chaotic route is further clarified by the enlargement, Figure 7(b). Grossly, the motion is quasi-periodic with periodic windows between the Hopf bifurcation point and Ω_5 beyond which chaos appears. Note, however, that there are narrow chaotic bands below Ω_5 where $\lambda_1 > 0$. In fact, around $\Omega \approx 2\cdot28$ the variation of λ_1 from Figure 7(a)
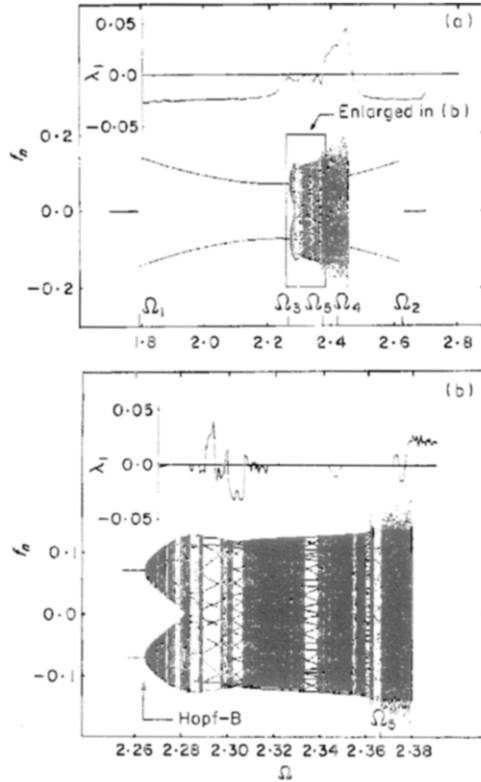
Figure 7. Bifurcations of antisymmetric amplitude f vs. excitation frequency Ω, for constant load $q=0\cdot2$. f is plotted at post-transient times $\tau_n=(n+3/4)2\pi/\Omega$, $n=1,1300$; λ_1; largest Lyapunov exponent; (b) is a $\times200$ magnification of a subrange of (a). ($\omega=2\cdot44$, $\beta=0\cdot03$, $m=3\cdot32$, $\kappa=2\cdot63$.)

repeats itself on a much smaller scale. This is the Ruelle–Takens–Newhouse (or quasi-periodic) route to chaos [21] by which a system turns chaotic after three subsequent Hopf bifurcations. Each Hopf bifurcation introduces a new basic frequency into the system. When, after the second Hopf bifurcation, there are two frequencies, these will generally be incommensurate, giving rise to quasi-periodic motion on a two-torus. The emergence of a third frequency after one additional Hopf bifurcation corresponds to motion on a three-torus, typically highly unstable, which decay into a strange attractor with finite probability.

The disappearance of chaotic solutions beyond Ω_4 in Figure 7(a) is associated with another mechanism. Decreasing Ω from the stable period-2 regime beyond Ω_4, transients moving on a strange attractor become increasingly long. In fact, some of the rightmost chaotic solutions of Figure 7(a) will settle down into stable period-2 solutions if the (very high) transient limit of 4000 forcing periods is raised even further. Thus, the boundary between chaotic and periodic motion in this region becomes blurred by the necessity of carrying out simulations (and laboratory experiments) in finite time. It has been conjectured by Grebogi et al. [21] that this so-called "transient route" to chaos is due to crises; that is, collisions between a chaotic attractor and a co-existing unstable periodic orbit.

We now turn to the determination of chaotic subregions in the (Ω, q) space covering the primary region of dynamic instability. In Figure 8(a) the regions corresponding to chaotic (black) or quasi-periodic (grey) motion is superimposed on the theoretically obtained stability diagram of Figure 5. The figure was obtained by computing the largest
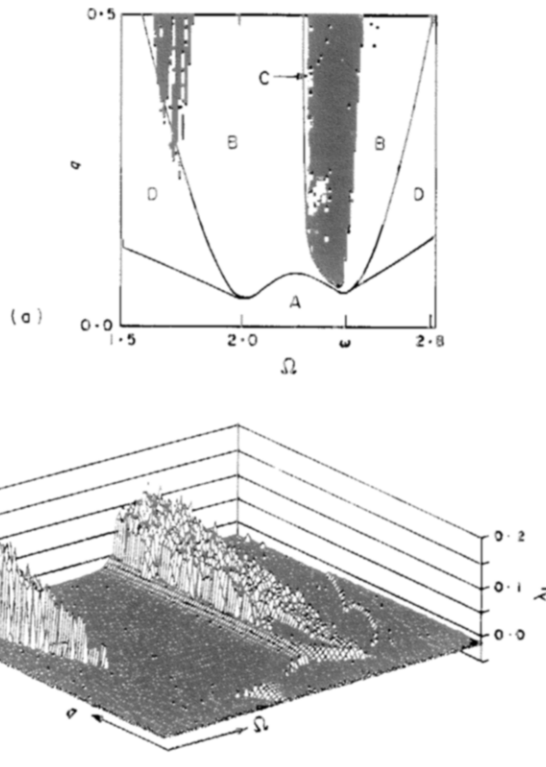
Figure 8. Regions of chaotic motion in the (Ω, q) parameter plane corresponding to the principal region of dynamical instability. ($\omega = 2 \cdot 44$, $\beta = 0 \cdot 03$, $m = 3 \cdot 32$, $\kappa = 2 \cdot 63$.) (a) Black zones correspond to chaos ($\lambda_1 > 0$), grey zones to quasi-periodic motion ($\lambda_1 \approx 0$); (b) magnitude of largest Lyapunov exponent λ_1.

Lyapunov exponents λ_1 on a 100×100 grid covering the (Ω, q) plane. The transient limit was set to 400 forcing periods, and average exponents were computed to two significant digits.

It appears that almost all solutions in the knife-shaped region C are chaotic, although there are minor periodic windows and a larger quasi-periodic region. It thus seems that the theoretically obtained instability region C serves as a rather accurate predictive criterion for the onset of chaotic and quasi-periodic motion. The extension of the chaotic region slightly beyond the right border of C is probably caused by the extremely long chaotic transients along this border. It also appears that there is a second region corresponding to chaotic solutions centred around $\Omega = 1 \cdot 7$ for $q \gtrsim 0 \cdot 25$. This region is discussed below. Magnitudes of the largest Lyapunov exponents λ_1 are presented in Figure 8(b), from which it appears that the positive exponents increase roughly in proportion to the load magnitude q. Note that $\lambda_1 = 0 \cdot 1$ implies that all information on initial conditions specified within one part per million is lost within 20 bits/(0·1 bits/s) = 200 (non-dimensional) seconds, corresponding to 48 to 89 forcing periods when $\Omega = 1 \cdot 5$ to $2 \cdot 8$.

The existence of the leftmost chaotic region of Figure 8(a) does not contradict the results of the theoretical perturbation analysis of section 3. Here it was shown that everywhere in region B the non-linear period-2 motion is *locally* stable. The numerical results show that in some regions of B this periodic motion is not *globally* stable; that is, persistent to arbitrarily large perturbations. A numerically obtained bifurcation diagram of a frequency sweep through this region for $q = 0 \cdot 3$ is shown in Figure 9. For 300 values of Ω, 4000 periods of the driving force were discarded as transients, before the next 300 values of f
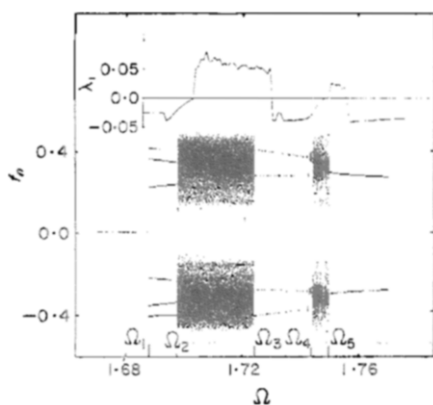
Figure 9. Bifurcations of stationary amplitude f vs. excitation frequency Ω when $q = 0.3$. f_n is the value of f at post-transient times $\tau_n = (n + \frac{1}{4})2\pi/\Omega$, $n = 1,1300$. λ_1 is the largest Lyapunov exponent. ($\omega = 2.44$, $\beta = 0.03$, $m = 3.32$, $\kappa = 2.63$.)

90° out of phase with the force were plotted. It appears that beyond $\Omega = \Omega_1$ the zero solution becomes unstable in favour of stable period-6 orbits. At Ω_2 these orbits turn chaotic, indicated by a positive Lyapunov exponent λ_1. Between Ω_3 and Ω_4 there are two stable period-2 attractors, of which the one actually reached depends on Ω. Beyond Ω_4 the response turns chaotic again, to be superseded by stable period-2 motion beyond Ω_5. Thus, in the range $\Omega_1 - \Omega_5$, which is small compared to the width of the primary region of dynamic instability, the theoretically predicted period-2 motion is not globally stable. A closer inspection of the routes to chaos revealed that the onset of chaos at Ω_2 occurs through a very short interval of quasi-periodic motion. The reappearance of periodic motion at Ω_3 is associated with transient chaos. (A typical strange attractor of the chaotic
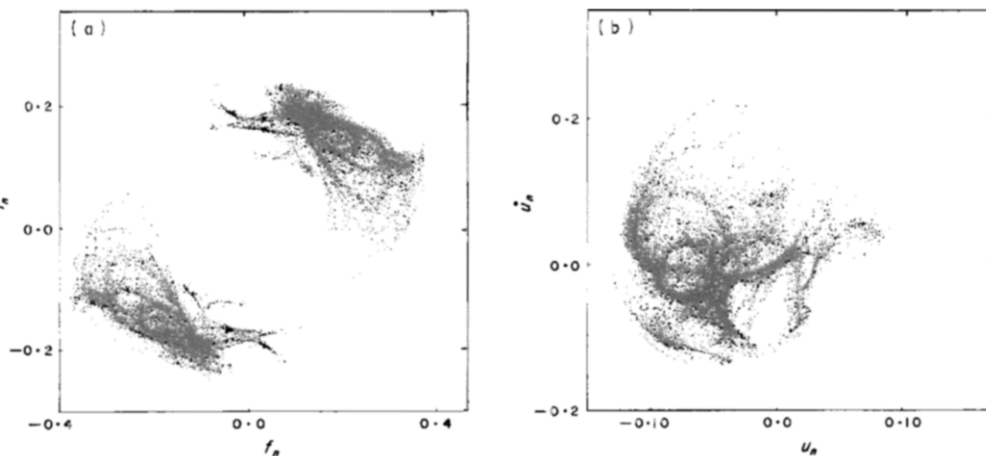

Figure 10. Poincaré sections of the strange attractor at $(\Omega, q) = (1.705, 0.3)$, sampled at $\tau_n = 2\pi n/\Omega$. Lyapunov dimension; $d_L = 3.7$. (a) $\dot{f}$ vs. f; (b) $\dot{u}$ vs. u. ($\omega = 2.44$, $\beta = 0.03$, $m = 3.32$, $\kappa = 2.63$.)

range $\Omega_2 - \Omega_3$ is shown in Figure 10.) The onset of chaotic motion at Ω_4 also occurs through the quasi-periodic route (note the finite interval of $\lambda_1 = 0$), while the disappearance of chaos at Ω_5 is associated with the phenomenon of chaotic intermittency [21]; that is, periods of regular periodic motion alternating with periods of chaotic motion. Just below Ω_5 the regular periods are very long (several hundred forcing cycles), while chaotic motion
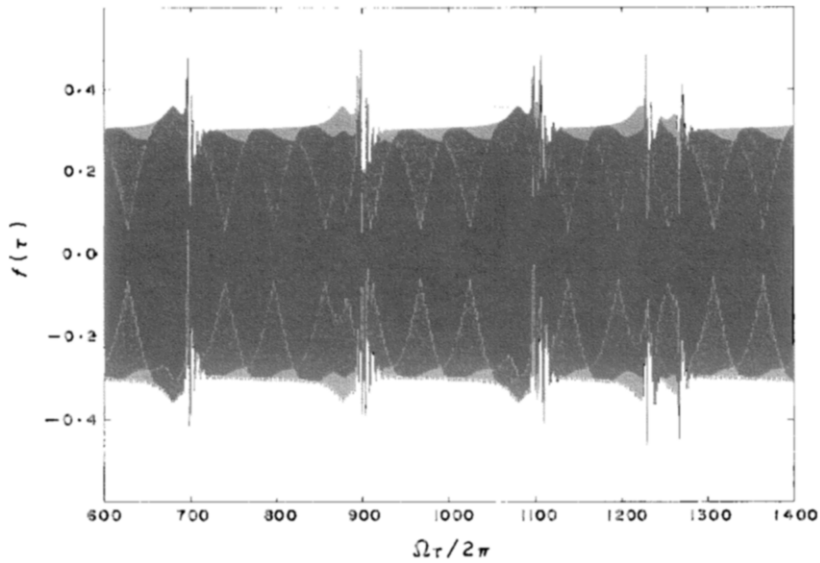
Figure 11. Post-transient time record of arch amplitude f for $(\Omega, q) = (1\cdot7496, 0\cdot3)$ showing chaotic intermittency. Time is given in number of forcing periods. ($\omega = 2\cdot44$, $\beta = 0\cdot03$, $m = 3\cdot32$, $\kappa = 2\cdot63$.)

occurs as sudden, short bursts (see Figure 11). Upon decreasing Ω further, the length of the regular periods decrease while the chaotic bursts get longer, until the motion is fully chaotic. The time instances of chaotic bursts appear randomly, and the intermittent motion is just as unpredictable as stationary chaotic motion.

In the preceding analysis, excitation frequency and magnitude (Ω, q) were considered to be the primary variables. Damping, initial conditions and arch opening span were fixed.

Increased damping affects the stability diagram (Figure 5) in two ways: the outer stability boundary is lifted upwards, and the knife-shaped region C shrinks and moves upwards. The latter effect is so pronounced that increasing β from 0·03 to 0·05 make region C disappear from the parameter space of Figure 5, while hardly changing the outer stability boundary. As chaos is primarily associated with region C, increased damping is in this case an effective guard against chaotic vibrations.

The influence of initial conditions was not examined in depth. A few changes corresponding to very small and very large initial disturbances were examined, without altering the general picture of Figure 8. However, initial conditions may of course be responsible to qualitative shifts in system behaviour, especially where multiple solution branches are possible, such as in the overhang region D of Figure 8 and the range $\Omega_3 - \Omega_4$ of Figure 9.

The effect of changing the arch opening span from $2a = 160°$ to $120°$ was examined, corresponding to $(\omega, m, \kappa) = (2\cdot30, 10\cdot73, 4\cdot77)$ instead of $(2\cdot44, 3\cdot32, 2\cdot63)$. The theoretical stability diagram of this case is qualitatively similar to that of Figure 5. Lyapunov exponents computed on a 30×30 grid resulted in a figure very similar to Figure 8, showing quasi-periodic and chaotic behaviour in the new region C, and an additional chaotic region along the left D–B border for high q.

5. SUMMARY

Non-shallow arches inherently possess a nearly two-to-one internal resonance between the second symmetric mode of vibration and the fundamental antisymmetric mode. The

fundamental mode may become strongly excited through non-linear interaction with an even weakly excited second mode. By perturbation analysis this was shown to take place in a rather wide frequency band of excitation around twice the fundamental linear natural frequency. A theoretical stability analysis showed that in a certain range of excitation frequency and magnitude, neither the zero solution nor any periodic solutions were locally stable. Numerical analysis showed that in this region quasi-periodic and chaotic motion were globally stable. An additional chaotic region along the left stability boundary was also located. Evidence for quasi-periodic and chaotic motion was given through Poincaré sections, frequency spectres and Lyapunov exponents. The chaos generating mechanisms were shown to include the transient route, the intermittency route and quasiperiodic break-up.

6. CONCLUSIONS

So far, most studies on structural chaotic vibration have dealt with strongly non-linear and heavily forced artificial structures, not encountered in engineering practice. The present study deals with a simple structure in widespread practical use, which according to numerical simulations may behave chaotically even at weak forcing in a finite frequency band.

Obviously, the results of this study should be tested experimentally. Lyapunov exponents can be estimated from experimentally measured time series, through the use of reconstructed attractors [20]. Thus essentially, a stability/chaos diagram such as Figure 8 should be obtained, on the basis of measured Lyapunov exponents.

It is suggested that the 1952–53 experiments of Bolotin [1] be repeated in order to fill this gap concerning chaotic vibration of arches.

REFERENCES

1. V. V. BOLOTIN 1964 *The Dynamic Stability of Elastic Systems* (translated by V. I. Weingarten *et al.*), San Francisco: Holden-Day.
2. F. C. MOON 1987 *Chaotic Vibrations.* New York: John Wiley.
3. R. W. LEVEN and B. P. KOCH 1981 *Physics Letters* **86A**(2), 71–74. Chaotic behaviour of a parametrically excited damped pendulum.
4. F. C. MOON, J. CUSUMANO and P. J. HOLMES 1987 *Physica* **24D**, 383–390. Evidence for homoclinic orbits as a precursor to chaos in a magnetic pendulum.
5. D. B. MOORE and S. W. SHAW 1990 *International Journal of Non-linear Mechanics* **25**(1), 1–16. The experimental response of an impacting pendulum system.
6. F. C. MOON 1980 *Journal of Applied Mechanics* **47**, 638–644. Experiments on chaotic motions of a forced nonlinear oscillator: strange attractors.
7. D. M. TANG and E. H. DOWELL 1988 *Journal of Applied Mechanics* **55**, 190–196. On the threshold force for chaotic motions for a forced buckled beam.
8. F. C. MOON and S. W. SHAW 1983 *International Journal of Non-linear Mechanics* **18**(6), 465–477. Chaotic vibrations of a beam with non-linear boundary conditions.
9. F. C. MOON and G. X. LI 1990 *American Institute of Aeronautics and Astronautics Journal* **28**(5), 915–921. Experimental study of chaotic vibrations in a pin-jointed space truss structure.
10. B. PODDAR, F. C. MOON and S. MUKHERJEE 1988 *Journal of Applied Mechanics* **55**, 185–189. Chaotic motion of an elastic-plastic beam.
11. M. P. PAÏDOUSSIS, G. X. LI and F. C. MOON 1989 *Journal of Sound and Vibration* **135**, 1–19. Chaotic oscillations of the autonomous system of a constrained pipe conveying fluid.
12. A. H. NAYFEH and R. A. RAOUF 1987 *Journal of Applied Mechanics* **54**, 571–577. Nonlinear forced response of infinitely long circular cylindrical shells.
13. E. H. DOWELL 1982 *Journal of Sound and Vibration* **85**, 333–344. Flutter of a buckled plate as an example of chaotic motion of a deterministic autonomous system.

14. W. SZEMPLINSKA-STUPNICKA, R. H. PLAUT and T.-C. HSIEH 1989 *Journal of Applied Mechanics* **56**, 947–952. Period doubling and chaos in unsymmetric structures under parametric excitation.

15. A. H. NAYFEH, B. BALACHANDRAN, M. A. COLBERT and M. A. NAYFEH 1989 *Journal of Applied Mechanics* **56**, 960–967. An experimental investigation of complicated responses of a two-degree-of-freedom structure.

16. C. P. PANTELIDES 1990 *Computers and Structures* **34**(5), 715–725. Computer-controlled structures.

17. J. HENRYCH 1981 *The Dynamics of Arches and Frames* (translated by R. Major). Amsterdam: Elsevier.

18. A. H. NAYFEH and D. T. MOOK 1979 *Nonlinear Oscillations*. New York: John Wiley.

19. A. H. NAYFEH 1989 in *Lasers, Molecules and Methods* (J. O. Hirschfelder, R. E. Wyatt and R. D. Coalsen, editors), 137–196. New York: John Wiley. Application of the method of multiple scales to nonlinearly coupled oscillators.

20. A. WOLF, J. B. SWIFT, H. L. SWINNEY and J. A. VASTANO 1985 *Physica* **16D**, 285–317. Determining Lyapunov exponents from a time series.

21. H. G. SCHUSTER 1989 *Deterministic Chaos*. Weinheim: VCH Verlagsgesellschaft.